PHYSICAL REVIEW B **110**, 035115 (2024)

Dual-band topological large-area waveguide transport in photonic heterostructures

Peng-Yu Guo,[1,2] Wei Li,[2] Junhui Hu,[2] and Hai-Xiao Wang[1,*]
[1]*School of Physical Science and Technology, Ningbo University, Ningbo 315211, China*
[2]*School of Physical Science and Technology, Guangxi Normal University, Guilin 541004, China*

(Received 11 February 2024; revised 13 May 2024; accepted 24 June 2024; published 8 July 2024)

Recent advances in all-dielectric topological photonics offer unprecedented opportunities for achieving robust waveguides. However, most topological waveguides are localized at small areas around the interfaces and usually operate in a single frequency window, leading to the low-throughput energy transmission over a narrow bandwidth. Here we report on the implementation of a dual-band topological large-area waveguide in heterostructures based on valley photonic crystals, in which the bandwidths are effectively widen by exploiting the dual-band topology. Inherited from the valley topology, the topological large-area waveguides exhibit the valley-locking effect at two separate frequency windows and are robust against sharp corners and defects. We also observe intriguing topological refractions of the topological large-area waveguides into the ambient space at zigzag and armchair terminations. Our work highlights both the tunable width and the large bandwidth of topological waveguides, paving the way for topological photonic integrated circuits with high performance and multifunctionality.

DOI: 10.1103/PhysRevB.110.035115

I. INTRODUCTION

Since Haldane and Raghu transferred the quantum Hall effect to the photonic systems [1,2], the topology study in photonics has attracted much attention and given birth to an emerging interdisciplinary study of topological photonics [3–7]. Different from frequency and polarization, topology provides an alternative degree of freedom to manipulate electromagnetic waves. A representative example is the topologically protected edge states featured with unidirectionality and backscattering immunity in photonic quantum Hall systems [8,9], which are highly desirable in guiding waves. Nevertheless, the realization of photonic quantum Hall systems usually relies on specific materials and requires the breaking of time-reversal symmetry. Hence, all-dielectric photonic topological crystalline insulators with time-reversal symmetry, which take full advantage of crystalline symmetry and get rid of material limitation, have attracted much attention [10–19]. To date, various photonic topological crystalline insulators with the different topological edge states, including photonic valley Hall insulators with topological kink states [14–16], photonic Z_2 topological insulators with pseudospin-dependent edge states [10–13], and photonic Floquet topological insulators with anomalous edge states [17–19], have been extensively studied.

Although all these topological edge states are beneficial for guiding waves, a common shortage is that only a small area around the strip boundary is utilized to collect and transfer energy and hence this limits the high-throughput robust energy transmission to a relatively low level. Very recently, a sandwichlike structure composed of valley sonic crystals was proposed to support large-area waveguide modes [20], providing a solution for achieving high-capacity energy transmission. Following this pioneering work, photonic unidirectional large-area waveguide modes [21–23] and valley-locked waveguide modes [24–26] were subsequently realized in heterostructures of topological photonic crystals (PhCs), largely advancing the manipulation of electromagnetic waves. Nevertheless, the operating bandwidth of these topological waveguides depends on the size of the band gap and the width of the waveguide. In particular, the operating bandwidth decreases rapidly as the waveguide's width increases [20–26]. It seems that large-width waveguide modes cannot have large operating bandwidths when using photonic topological heterostructures, which hinders their application in broadband photonic devices. On the other hand, owing to the bosonic nature of photons, photonic topological phenomena can involve multiple band gaps, leading to multiple-band topology [27–34]. For example, photonic topological edge states can exist at two separate frequency windows, which may enable multiplexing of topological edge states [27,30–34] and edge-enhanced resonant nonlinear photonic effects [28,29]. In fact, topological photonics with multiple topological band gaps provide an effective way to enlarge the working frequency window of topological edge states and are beneficial for the design of multifunctional photonic devices.

Inspired by multiple band topology, here we propose a dual-band topological waveguide in the heterostructure of valley PhCs, in which both the tunable mode width and the extended working bandwidth of the topological waveguide are addressed. The heterostructures consisting of three domains of PhCs, namely, a PhC with Dirac points sandwiched by two PhCs with different valley topologies, supporting a topological large-area waveguide with a tunable mode width at two separated band gaps. Inherited from the topological

---

[*] Contact author: wanghaixiao@nbu.edu.cn

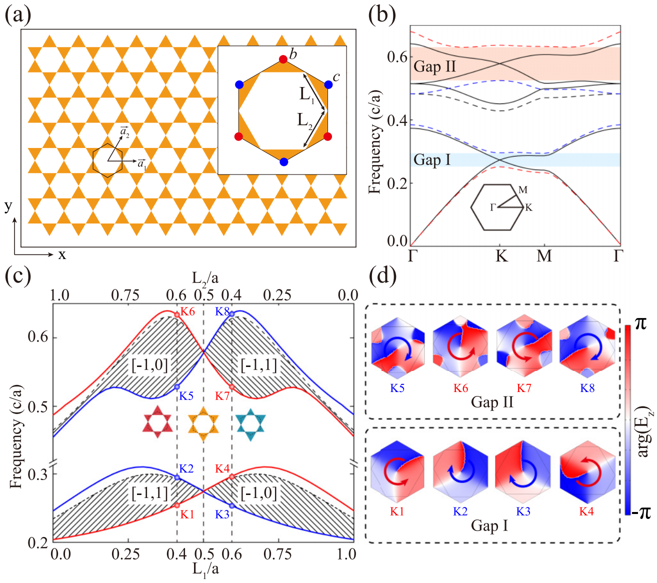

FIG. 1. (a) Schematic of two-dimensional hexagonal PhCs consisting of triangular dielectric rods. $\vec{a}_1$ and $\vec{a}_2$ refer to the lattice translation vectors. Inset: Zoom-in of the unit cell. L_1 and L_2 are the side lengths of two triangular rods. (b) Photonic band structures of PhC-B (solid lines) with $L_1 = L_2 = 0.5a$ and PhC-A (dashed lines) with $L_1 = 0.4a$ and $L_2 = 0.6a$. Inset: The first Brillouin zone. (c) Evolution of gaps I and II (shaded areas) as well as the frequencies of the first, second, fourth, and fifth bands at the K point (colored by solid lines) versus L_1 and L_2. (d) Phase distributions of the electric field E_z at points $K1$–$K4$ for gap I (lower panel) and points $K5$–$K8$ for gap II (upper panel). The anticlockwise (clockwise) phase-winding directions indicated by red (blue) arrows give rise to the C_3 symmetry eigenvalue of $e^{i\frac{2\pi}{3}}$ ($e^{i\frac{4\pi}{3}}$).

kink states in the valley PhCs, both large-area waveguide modes at two separated band gaps exhibit the valley-locking effect and are robust against the sharp corners and defects. We further explore the refraction behaviors when the topological large-area waveguide enters into the ambient space at the zigzag/armchair termination at different working frequencies.

II. RESULTS AND DISCUSSION

A. Dual-band valley photonic crystals

To start, we first consider a two-dimensional hexagonal PhC consisting of equilateral triangle dielectric rods. As shown in Fig. 1(a), each unit cell is composed of six triangular dielectric rods with relative permittivity $\epsilon = 13$, of which the centers coincide with the corners of the unit cell. Specifically, these dielectric rods are divided into two groups according to the maximal Wyckoff positions of C_3 symmetry. As indicated by the red and blue dots, the side length of the dielectric rods located at c and b are denoted as L_1 and L_2, respectively, and the summation of L_1 and L_2 is equal to the lattice constant a. It is obvious that the crystalline symmetry is closely related to the geometric ratio L_1/L_2. For concreteness, we consider three typical PhCs with $L_1 = 0.4a$, $0.5a$, and $0.6a$, denoted as PhC-A, PhC-B, and PhC-C, respectively. Throughout this work, we only consider the transverse-magnetic modes, and all simulations are carried out with the radio-frequency module of the commercial software COMSOL MULTIPHYSICS.

In Fig. 1(b), we present the photonic band structures of PhC-B and PhC-A, which are plotted with solid and dashed lines, respectively. It is seen that two Dirac points protected by C_{3v} symmetry emerge at the K point at different frequencies for PhC-B, while for PhC-A, the C_{3v} symmetry breaking leads to the degeneracy lift of Dirac points and the formation of two band gaps, i.e., gaps I and II [see the light blue and red areas of Fig. 1(b)]. On the other hand, it is evident that PhC-A has the same band structure as PhC-C since they are mirror symmetric with respect to the x axis. Nevertheless, they have different band topologies, as we elaborately discuss later.

To show the topological phase transition, we plot the frequency range of gaps I and II (see the shaded areas) as well as the frequencies of the first, second, fourth, and fifth bands at the K point the (see the colored solid lines) versus L_1 and L_2 in Fig. 1(c). It is obvious that both gaps I and II experience a process of closing and reopening accompanying the increasing (decreasing) of L_1 (L_2). In general, the topological phase transition in an all-dielectric photonic crystalline insulator can be captured by the symmetry reduction and restoration. Here we utilize the topological index, which can be read from the eigenvalue of the crystalline symmetry and serves as a well-defined topological invariant [35], to characterize the gap topology. According to Ref. [35], the topological index for a crystalline insulator with C_3 symmetry is given by $\chi = ([K_1], [K_2])$, where $[K_1]$ ($[K_2]$) refers to the number of band differences between the K and Γ points with C_3 eigenvalues of 1 ($e^{i\frac{2\pi}{3}}$) below a specific band gap. As an illustration, we present the phase distributions of eigenstates $K1$ to $K8$ in Fig. 1(d), in which the phase-winding directions are indicated by the arrows. Note that the anticlockwise and clockwise phase-winding directions indicate the band at the K point has C_3 symmetry eigenvalues of $e^{i\frac{2\pi}{3}}$ and $e^{i\frac{4\pi}{3}}$, respectively. Hence, for gap I, the eigenstates $K1$ and $K4$ ($K2$ and $K3$) feature anticlockwise (clockwise) phase-winding directions, giving rise to $[-1, 1]$ for PhC-A and $[-1, 0]$ for PhC-C. In contrast, for gap II, the eigenstates $K5$ and $K8$ ($K6$ and $K7$) feature clockwise (anticlockwise) phase-winding directions, and hence the topological indexes for PhC-A and PhC-C are $[-1, 0]$ and $[-1, 1]$, respectively. Note that the topological phases and the phase transition process in Fig. 1(c) can also be captured by the effective Hamiltonian with massive/massless Dirac terms (see Appendix A).

B. Design of topological large-area waveguide

We then construct a heterostructure by placing the three domains A, B, and C together, which consists of PhC-A, PhC-B and PhC-C, respectively [see Fig. 2(a)]. To simplify, such heterostructures are denoted as $A|B_x|C$ and x refers to the layer number of domain B. Note that the previous studies have focused on the domain wall formed by $A|C$, which supports the topological kink states around K and K' [14–16,27]. In Figs. 2(b) and 2(c), we display the eigenspectra of the heterostructures $A|B_{10}|C$ at different frequency ranges by implementing the eigencalculation. It is seen that, for both gaps I and II, a gapless band indicated by the red line, transverses

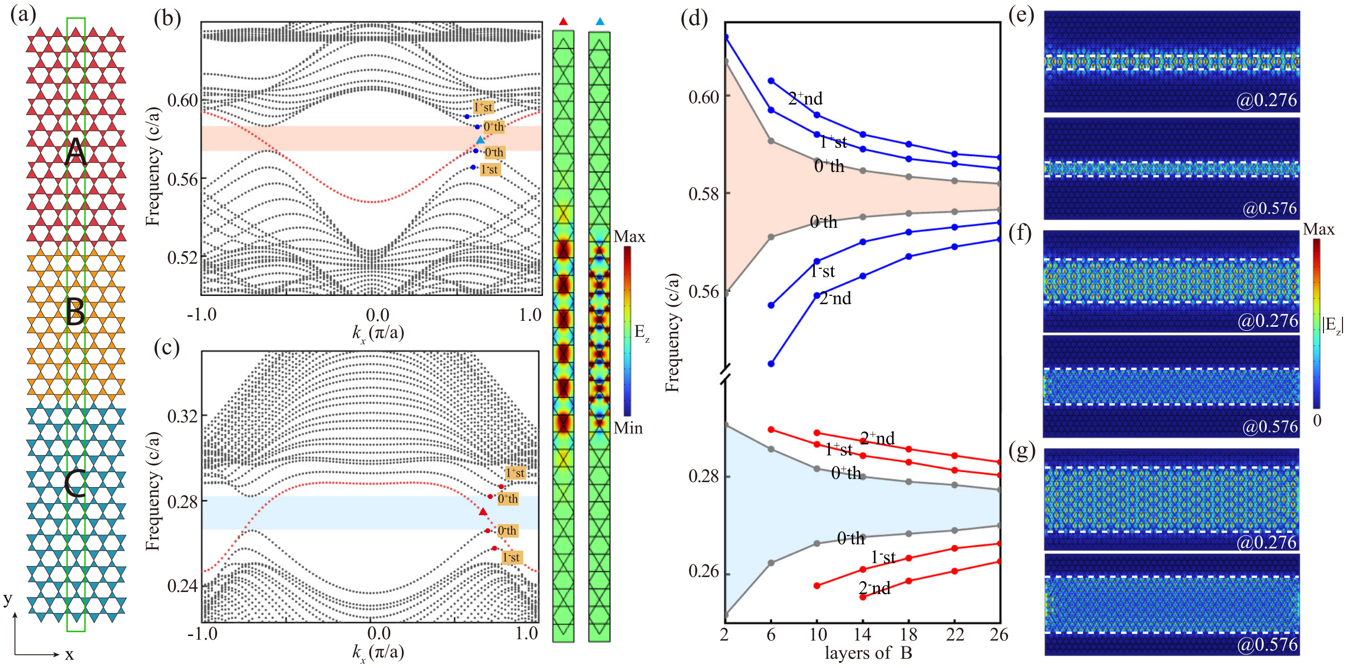

FIG. 2. (a) Schematic of heterostructure $A|B_x|C$ formed by PhC-A, PhC-B, and PhC-C. (b), (c) Projected band structure of heterostructure $A|B_{10}|C$, in which the large-area waveguide and other guiding modes are clearly seen in (b) gap I and (c) gap II. Right panel: Two typical eigen electric field patterns E_z of the topological large-area waveguide with high frequency and lower frequency at the K point. (d) Evolution of the bandwidth of the large-area waveguide versus the layer of domain B. (e)–(g) Electric field pattern of heterostructure $A|B_x|C$ with (e) $x = 2$, (f) $x = 6$, and (g) $x = 10$, respectively, where the upper (lower) panel refers to the topological large-area waveguide at a frequency of $0.276\frac{c}{a}$ ($0.576\frac{c}{a}$).

at the K and K' points the entire bulk gap of domains A and C, serving as a robust waveguide mode at two distinct frequency ranges. Moreover, for gap I (II), the gapless waveguide modes host a positive (negative) group velocity at the K point and a negative (positive) group velocity at the K' point. These bands are very similar to the topological kink states in the domain wall structure $A|C$. In fact, it is demonstrated that the large-area waveguide mode could be regarded as a combination of the valley kink states in the domain wall $A|C$ and the bulk states in domain B (see Appendix B). Hence, it is predicted that the topological large-area waveguides inherit all the topological features of valley kink states like the valley-momentum locking effect [24].

To visualize the topological large-area waveguide modes, we further display two typical electric field patterns (indicated by red and blue triangles) of gapless bands in the right panel of Fig. 2(b). In contrast to the topological kink states between $A|C$, the waveguide modes within both gaps I and II extended into the entire domain B, verifying that gapless bands within the gaps I and II are indeed the large-area waveguide modes featured with valley-momentum locking. In addition to these gapless bands, we also notice there exist other guiding wave bands, denoted by 0^+th, 0^-th, 1^+st, and 1^-st, within gaps I and II. However, all these bands are gapped and, therefore, do not have the topological origin.

Moreover, since the width is another degree of freedom to design the high-performance waveguide, we further study the width of domain B on the bandwidth of large-area waveguide modes. As shown in Fig. 2(d), the topological large-area waveguide modes within higher- and lower-frequency windows decrease accompanied by the increase of the layer number of domain B, as demonstrated in Ref. [20]. Nevertheless, we remark that the reduction in a single bandwidth due to the increase in the layer number of PhC-B can be compensated by introducing the dual-band and even multiband topological PhCs configurations. On the other hand, the increasing of the layer number of PhC-B does not affect on the transmission property of the large-area waveguide. To prove it, we present the normalized electric field patterns of the topological large-area waveguide modes at frequencies of $0.276\frac{c}{a}$ and $0.576\frac{c}{a}$, with the layer number of domain B being equal to 2, 6, and 10, respectively, in Figs. 2(e)–2(g). It is observed that all these large-area waveguide modes exhibit nearly perfect transmission.

C. Robustness of topological large-area waveguides

Inspired by the robustness of valley kink states in the $A|C$ domain wall systems, it is expected that the topological large-area waveguide inherits the same features from the valley kink states. To this end, we design a Ω-shaped large-area waveguide of heterostructure $A|B_{10}|C$ to simulate the waveguide bend. In addition, we also study the transmission performance of the straight large-area waveguide with and without random disorders. In simulations, we utilize the point sources (see green dots) to excite large-area waveguide modes. Owing to the impedance mismatch between the excitation wave and the large-area waveguide mode, the transmissions are lower than unity. Nevertheless, the nontrivial topological physics of the large-area waveguide can be verified by comparing its

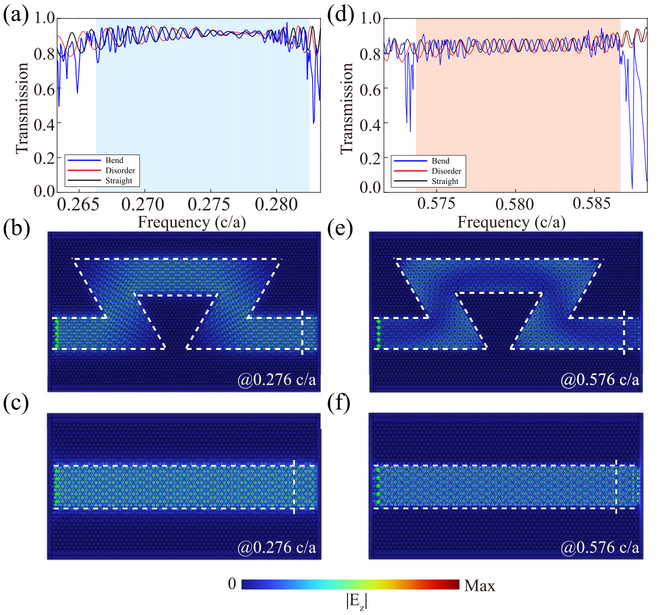

FIG. 3. (a), (d) Transmission of straight large-area waveguide (black line) transmission of large-area waveguide with Ω configuration (blue line) and with defects (red line), of which the frequency is within (a) gap I and (d) gap II, respectively. (b), (e) Simulated electric field pattern of large-area waveguide with Ω configuration at a frequency of (b) $0.276\frac{c}{a}$ and (e) $0.576\frac{c}{a}$ under point excitation. (c), (f) Simulated electric field pattern of large-area waveguide with defects at a frequency of (c) $0.276\frac{c}{a}$ and (f) $0.576\frac{c}{a}$ under point excitation.

transmission behavior in different situations. For the topological large-area waveguide modes within the lower-frequency window, it is seen that transmission of the straight waveguide is nearly the same as that in the presence of sharp corners and defects in Fig. 3(a). Furthermore, the nice uniform distribution of the normalized electric field patterns at a frequency of $0.276\frac{c}{a}$, in Figs. 3(b) and 3(c), also demonstrates the robustness aspect of the large-area waveguide modes. Similarly, for the topological large-area waveguide modes within higher-frequency windows, we get similar conclusions by checking both transmission spectra [see Fig. 3(d)] and simulated electric field patterns of the Ω-shaped large-area waveguide [see Fig. 3(e)] and the straight large-area waveguide with defects [see Fig. 3(f)] at a frequency of $0.576\frac{c}{a}$. Moreover, we also demonstrate the large-area waveguides have good fabrication tolerance by implementing the disorder-robust testament in Appendix C.

By utilizing the topological large-area waveguide, we further construct two types of channel intersections to explore intriguing wave routing effects. As schematically marked by the dashed lines in Figs. 4(a) and 4(b), both the left and right heterostructures are in the order of $A|B|C$ (denoted as type-I), while that in Figs. 4(d) and 4(e), the left (right) heterostructures are in the order of $A|B|C$ ($C|B|A$) (denoted as type-II). Note that four ports labeled as 1 to 4 are used for wave routing and the transmissions from port j to port i are labeled as S_{ij}. To illustrate the performance of type-I channel intersection, we placed the point sources at port 1 and excited topological large-area waveguide modes at frequencies of $0.276\frac{c}{a}$ (within the gap I) and $0.576\frac{c}{a}$ (within the gap II), respectively. The excitation settings are the same as those in Fig. 3. It is seen from the simulated electric fields in Figs. 4(a) and 4(b) that the topological large-area waveguide modes excited at port 1 propagate to port 2 directly, which can be further verified by the transmission in Fig. 4(c). Moreover, it is also seen that S_{31} and S_{41} experience a sudden increase at a higher-frequency range of both gaps I and II. Note that the topological large-area waveguide modes featuring the valley-momentum locking effect originated from the valley kink states formed by two valley PCs, which are described by the effective Hamiltonian with massive Dirac terms around the $K(K')$ point. Hence, a large deviation from the $K(K')$ point, or the frequency of the Dirac point, results in the approximation of the theoretical model no longer being valid, which in turn invalidates the

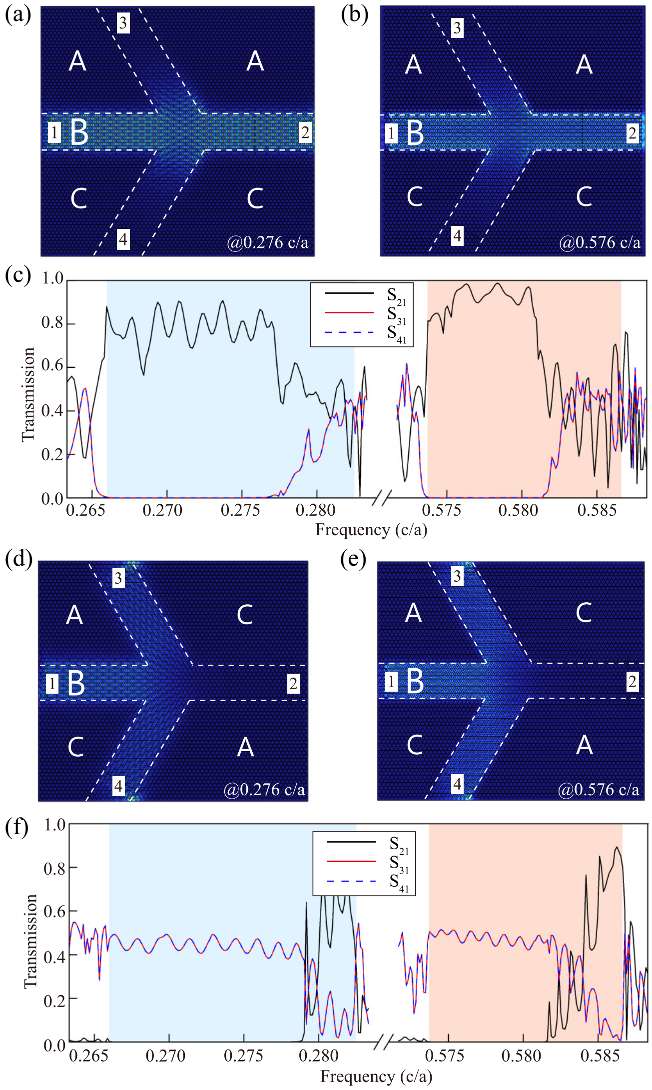

FIG. 4. (a), (b) Simulated electric field of type-I topological channel intersections at a frequency of (a) $0.276\frac{c}{a}$, and (b) $0.576\frac{c}{a}$. (c) Transmission spectra of type-I topological channel intersections. (d), (e) Simulated electric field of type-II topological channel intersections at a frequency of (a) $0.276\frac{c}{a}$, and (b) $0.576\frac{c}{a}$. (f) Transmission spectra of type-II topological channel intersections.

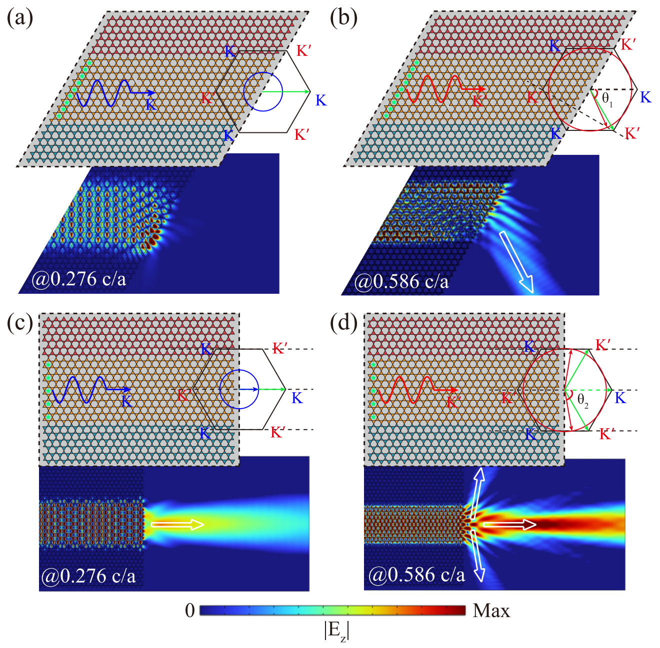

FIG. 5. (a), (b) Schematic of the outcoupling of the large-area waveguide mode projected from the K valley through the zigzag terminations at a frequency of (a) $0.276\frac{c}{a}$ and (b) $0.586\frac{c}{a}$ based on the phase-matching condition. Bottom insets are the corresponding simulated normalized electric field. (c), (d) Same as panels (a) and (b) except that the termination is the armchair type.

valley-momentum locking effect in the topological large-area waveguide.

In addition, for the type-II channel intersection, the launched topological waveguide modes are suppressed in port 2 and output from ports 3 and 4 [see Figs. 4(d) and 4(e)]. This is because the transport route from port 1 to port 2 has the same valley, while the transport routes from port 1 to ports 3 and 4 have the opposite valley. The transmission spectra in Fig. 4(f) show that S_{31} and S_{41} are nearly equivalent to each other (approximately 0.5) owing to the symmetric structure, namely, the energy from the input is equally separated into two routes, and are larger than S_{21} within the lower- and higher-frequency windows, which are in a good agreement with the normalized electric field in Figs. 4(d) and 4(e). It is also noteworthy that S_{31} and S_{41} are lower than S_{21} in lower- and higher-frequency ranges of both gaps I and II, indicating the breakdown of the valley-momentum locking effect. This is because the frequencies of those states deviate significantly from that of the Dirac point, making the approximation of the effective Hamiltonian no longer satisfied, which in turn breaks down the valley-momentum locking effect in the topological large-area waveguide.

D. Topological refraction of the large-area waveguide mode

To further exploit the potential application, we study the refraction behavior of the large-area waveguides in the free space. Here we first consider the refraction behavior of the large-area waveguide modes in the ambient space at the zigzag termination [see Figs. 5(a) and 5(b)]. It is expected that the direction of the outgoing beam into air depends on the type of valley from which the large-area waveguide modes are projected. According to the projected band structures in Figs. 2(b) and 2(c), the large-area waveguide modes that propagate from left to right (the group velocity is positive) within lower (higher) frequency are projected from the $K(K')$ valley, in which the value of wave vector is $|\boldsymbol{K}| = \frac{4\pi}{3a}$. Besides, the wave vector in free space can be read from the equifrequency curve in the air, namely, $|\boldsymbol{k}| = \frac{2\pi f}{c}$.

To illustrate the refraction behavior with zigzag termination, we draw the equifrequency curves in free space and the first Brillouin zone on a scale that represents the relative magnitudes of the wave vectors of the incident and refraction waves. By applying the phase-matching condition, i.e., $\boldsymbol{k} \cdot \boldsymbol{e}_{\mathrm{zig}} = \boldsymbol{K} \cdot \boldsymbol{e}_{\mathrm{zig}}$, to the termination interface parallel to $\boldsymbol{e}_{\mathrm{zig}}$, it is possible to quantitatively obtain the refraction angle of the output beams. It is noteworthy that the above equation has no solution when $|\boldsymbol{k}| < |\boldsymbol{K}| \cos 60^\circ$. In other words, the large-area waveguide mode at a frequency of $0.276\frac{c}{a}$, of which the frequency f is smaller than the cutoff frequency $f_c = \frac{c}{3a}$, cannot refract into the free space. As expected, the simulated normalized electric field in Fig. 5(a) indicates that the large-area waveguide mode cannot output into the free space and has to be localized at the zigzag termination, which may find potential application in the photonic cavity [36]. In contrast, the large-area mode emerges and will be refracted into the free space when the frequency of the incident wave $f > f_c$. As an example, the refraction angle θ_1 in Fig. 5(b) can be calculated by $|\boldsymbol{k}| \cos(120^\circ - \theta_1) = |\boldsymbol{K}| \cos 60^\circ$, which gives rise to a refraction angle of 64.7° at a frequency of $0.586\frac{c}{a}$. The simulated result in Fig. 5(b) is in good agreement with the theoretical analysis.

Following the above analysis, we then consider the large-area waveguide modes in the ambient space at the armchair termination [see Figs. 5(c) and 5(d)]. By applying the phase-matching condition, the large-area waveguide mode excited at the K valley at a frequency of $0.276\frac{c}{a}$ will be refracted vertically into free space [see Fig. 5(c)]. On the other hand, for the excited large-area waveguide at a frequency of $0.586\frac{c}{a}$, the applying of the phase-matching condition shall result in two refracted waves into the free space, of which both refraction angles θ_2 are 80.3°. Nevertheless, the simulated result shows another refracted wave vertically output into the free space. This is because that armchair-type termination introduces strong intervalley scattering and produces significant unwanted diffraction [14]. Hence, we demonstrate that the large-area waveguide modes within lower- and higher-frequency windows host different refraction behaviors.

III. CONCLUSION

To conclude, we propose a heterostructure made up of dual-band valley PhCs to realize dual-band photonic topological waveguides. Inherited from the valley topology, the waveguides featuring valley-momentum locking are robust against sharp corners and defects. Owing to the bosonic nature of photons, the topological waveguide can survive in two separate band gaps and hence effectively extend the operating bandwidth. Based on the double valley-locking phenomena, we point out that topological waveguides within lower- and higher-frequency ranges host different refraction behaviors.

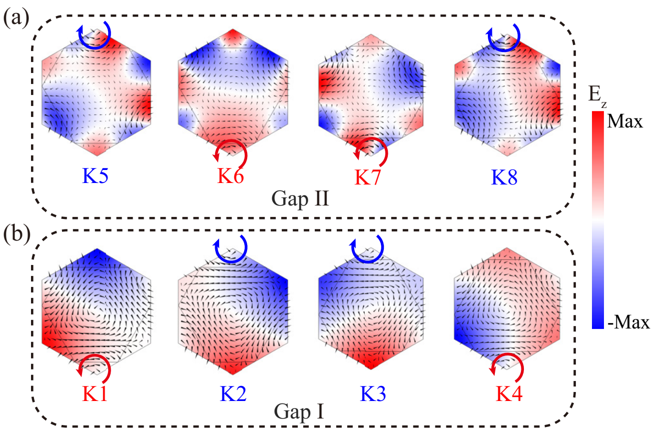

FIG. 6. The corresponding electric field pattern and energy flow distributions of (a) $K5$ to $K8$ and (b) $K1$ to $K4$.

Last but not least, it is also interesting to explore dual-band or even multiband topological large-area waveguide modes based on other topological photonics, e.g., photonic quantum Hall or spin Hall insulators.

ACKNOWLEDGMENTS

The authors are thankful for support from the Natural Science Foundation of Guangxi Province (Grant No. 2023GXNSFAA026048), the faculty startup funding of Ningbo University, and the National Natural Science Foundation of China (Grant No. 11904060).

APPENDIX A: EFFECTIVE HAMILTONIAN WITH MASSIVE/MASSLESS DIRAC TERM AROUND THE *K* VALLEY

We first present the field patterns of $K1$ to $K8$ with energy flow distributions in Fig. 6. It is seen that these energy flow distributions display typical vortex profiles centered at the two inequivalent Wyckoff positions b and c, which further can be viewed as pseudospins analogous to A-B sublattice in a graphene system. For example, eigenstates $K1$ and $K4$ ($K2$ and $K3$) exhibit anticlockwise (clockwise) energy flow centered at Wyckoff position $c(b)$ [see Fig. 6(b)]. We then label eigenstates that exhibit anticlockwise energy flow centered at Wyckoff position c and clockwise energy flow centered at Wyckoff position b at the ith gap as ϕ_{c+}^i and ϕ_{b-}^i, respectively.

Hence, the topological phase transition in Fig. 1(c) can be also captured by the effective Hamiltonian around the K valley [15],

$$\delta H_K^i = v_{Di}(\delta k_x\sigma_x + \delta k_y\sigma_y) + m_i v_{Di}^2\sigma_z, \tag{A1}$$

in the Hilbert space spanned by the vortex pseudospin (ϕ_{c+}^i, ϕ_{b-}^i). Note that the effective Dirac Hamiltonian around the K' valley can be obtained by applying the time-reversal operation. Here $\delta\mathbf{k} = \mathbf{k} - \mathbf{k_K}$ refers to the displacement of the wave vector $\mathbf{k}$ away from the K valley in the momentum space, v_{Di} is the group velocity of the ith gap, σ_j ($j = x$, y, and z) are the Pauli matrices, and m_i is the effective mass term of the ith gap (which is dependent on the ratio L_1/L_2). Specifically, the effective mass is proportional to the frequency difference between ϕ_{c+}^i and ϕ_{b-}^i, namely,

$$m_i = \frac{\omega_{c+}^i - \omega_{b-}^i}{2v_{Di}^2}, \tag{A2}$$

where ω_{c+}^i and ω_{b-}^i refer to the eigenfrequencies of eigenstates ϕ_{c+}^i and ϕ_{b-}^i, respectively. Hence, we have $m_I < 0$ and $m_{II} > 0$ for PhC-A, $m_I = m_{II} = 0$ for PhC-B, and $m_I > 0$ and $m_{II} < 0$ for PhC-C. For convenience, we introduce two positive parameters, $M_I > 0$ and $M_{II} > 0$, and let $m_{C,I} = M_I$ and $m_{A,II} = M_{II}$. Then, according the phase transition diagram, we have $m_{A,I} = -m_{C,I} = -M_I < 0$ and $m_{A,II} = -m_{C,II} = M_{II} > 0$.

APPENDIX B: EXPLANATION OF THE LARGE-AREA WAVEGUIDE MODE IN PHOTONIC HETEROSTRUCTURES

Here we prove that the topological large area in our work could be regarded as a combination of the valley kink states in the domain wall $A|C$ and the bulk states in domain B. We take the large-area waveguide modes in gap I as an illustration. By solving the eigenvalue equation $\delta H_K^I\psi = \delta\omega$, the dispersion relation can be derived as

$$\delta^2\omega = v_{DI}^2(\delta^2 k_x + \delta^2 k_y) + M_I^2 v_{DI}^2. \tag{B1}$$

Suppose that the thickness of domain B is L, the $A|B$ interface is located at $y = L/2$ and the $B|C$ interface is located at $y = -L/2$. According to the field pattern of the large-area mode, it is seen that the exponential attenuates along the $+y$ $(-y)$ direction in domain $A(C)$, which requires

$$k_y = \begin{cases} \dfrac{i\sqrt{v_{DI}^2\delta^2 k_x + M_I^2 v_{DI}^4 - \delta^2\omega}}{v_{DI}}, & y > \dfrac{L}{2}, \\[2ex] -\dfrac{i\sqrt{v_{DI}^2\delta^2 k_x + M_I^2 v_{DI}^4 - \delta^2\omega}}{v_{DI}}, & y < -\dfrac{L}{2}. \end{cases} \tag{B2}$$

It is evident that a specific solution with $\delta\omega = v_D\delta k_x$ and $\psi_{ABC} = (1, 1)^T$, or in coordination with representation

$$\psi_{ABC} \propto \begin{cases} e^{i\delta k_x x}e^{-M_I v_{DI}(y-\frac{L}{2})}, & y > \dfrac{L}{2}, \\[2ex] e^{i\delta k_x x}, & \dfrac{L}{2} \geqslant y \geqslant -\dfrac{L}{2}, \\[2ex] e^{i\delta k_x x}e^{M_I v_{DI}(y+\frac{L}{2})}, & y < -\dfrac{L}{2}, \end{cases} \tag{B3}$$

can easily be identified, which satifies $\delta H_K\psi = \delta\omega\psi$ in all domains and is continuous at their boundaries. The calculated velocity of the topological large-area waveguide mode is the same as that of the bulk waves in domain B, indicating that the large-area waveguide mode can only propagate along $+x$ due to the positive slope.

APPENDIX C: DISORDER-ROBUSTNESS TESTAMENT

According to the symmetry requirement and Fig. 1, the Dirac point in domain B forms only at $L_1 = L_2$. Nevertheless, the small fluctuations between L_1 and L_2 in domain B do not disrupt the nice uniform distribution of the electric field. To prove it, we implement a transmission testament of the

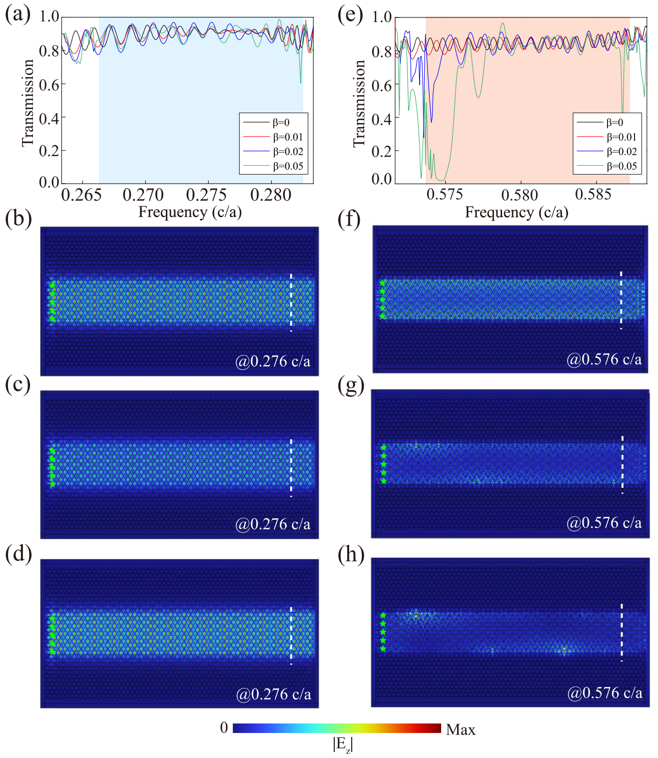

FIG. 7. (a), (e) The transmission of straight topological large-area modes in the presence ($\beta \neq 0$)/absence ($\beta = 0$) of disorders for (a) gap I and (e) gap II, respectively. Typical normalized electric field patterns of topological large-area modes at frequencies of (b)–(d) $0.276\frac{c}{a}$ and (f)–(h) $0.576\frac{c}{a}$ with (b), (f) $\beta = 0.01$, (c), (e) $\beta = 0.02$, (d), (h) $\beta = 0.05$.

topological large-area waveguide in the presence/absence of small fluctuations of PhC-B, in which the small fluctuations are created by introducing the side length of PhC-B randomly. We define the side length disorder as $\delta_i = \beta\xi_i a$, where β refers to the side length disorder factor determining the overall degree of disorder, $\xi_i \in [-1, 1]$ is a random number that follows a standard normal distribution, namely, $\xi_i \sim N(0, 1)$, and the subscript i is the order of the triangular dielectric rod in domain B. We then calculate the transmission of topological large-area waveguide modes in the presence of small fluctuations of the side length in PhC-B. We consider three situations, i.e., $\beta = 0.01$, 0.02, and 0.05 to simulate different side length fluctuations. The results are presented in Fig. 7. Compared with the transmission of straight topological large-area waveguide modes, it is seen that the transmission of topological large-area waveguide modes in the presence of small fluctuations, e.g., $\beta = 0.01$, indicated by red lines in Figs. 7(a) and 7(e), nearly remains unchanged for both gaps I and II. Moreover, the typical normalized electric field patterns [see Figs. 7(b) and 7(f)] also indicate that the small fluctuations of side length in domain B do not disrupt the uniform field distribution. Interestingly, increasing the side length disorder factor β to 0.02 and eventually to 0.05 makes a difference in the large-area waveguide in lower- and higher-frequency windows. For large-area waveguide modes working in gap I, it is seen that large disorder fluctuations do not affect the spectra too much [see blue and green lines in Fig. 7(a)] and the electric field pattern nearly remains unchanged [see Figs. 7(c) and 7(d)]. However, for large-area waveguide modes working in gap II, the added large disorder fluctuations result in significant decrease of the transmission [see the blue and green lines in Fig. 7(e)] at the edges of frequency windows and destroy the uniform electric fields [see Figs. 7(g) and 7(h)].

Overall, these results suggest that our large-area waveguides have good fabrication tolerance in the case of small fluctuations. Hence, we claim that domain B provides a width degree of freedom that supports high-throughout robust energy transmissions that are superior to the conventional interface formed by PhC-A and PhC-C.

[1] S. Raghu and F. D. M. Haldane, Analogs of quantum-Hall-effect edge states in photonic crystals, Phys. Rev. A **78**, 033834 (2008).

[2] F. D. M. Haldane and S. Raghu, Possible realization of directional optical waveguides in photonic crystals with broken time-reversal symmetry, Phys. Rev. Lett. **100**, 013904 (2008).

[3] T. Ozawa, H. M. Price, A. Amo, N. Goldman, M. Hafezi, L. Lu, M. C. Rechtsman, D. Schuster, J. Simon, O. Zilberberg, and I. Carusotto, Topological photonics, Rev. Mod. Phys. **91**, 015006 (2019).

[4] M. Kim, Z. Jacob, and J. Rho, Recent advances in 2D, 3D and higher-order topological photonics, Light: Sci. Appl. **9**, 130 (2020).

[5] H. Xue, Y. Yang, and B. Zhang, Topological valley photonics: physics and device applications, Adv. Photonics Res. **2**, 2100013 (2021).

[6] G.-J. Tang, X.-T. He, F.-L. Shi, J.-W. Liu, X.-D. Chen, and J.-W. Dong, Topological photonic crystals: physics, designs, and applications, Laser & Photon. Rev. **16**, 2100300 (2022).

[7] H.-X. Wang and J.-H. Jiang, A short review of all-dielectric topological photonic crystals, Front. Phys. **10**, 866552 (2022).

[8] Z. Wang, Y. D. Chong, J. D. Joannopoulos, and M. Soljačić, Reflection-free one-way edge modes in a gyromagnetic photonic crystal, Phys. Rev. Lett. **100**, 013905 (2008).

[9] Z. Wang, Y. D. Chong, J. D. Joannopoulos, and M. Soljačić, Observation of unidirectional backscattering-immune topological electromagnetic states, Nature (London) **461**, 772 (2009).

[10] L.-H. Wu and X. Hu, Scheme for achieving a topological photonic crystal by using dielectric material, Phys. Rev. Lett. **114**, 223901 (2015).

[11] Y. Yang, Y. F. Xu, T. Xu, H.-X. Wang, J.-H. Jiang, X. Hu, and Z. H. Hang, Visualization of a unidirectional electromagnetic waveguide using topological photonic crystals made of dielectric materials, Phys. Rev. Lett. **120**, 217401 (2018).

[12] L. Xu, H.-X. Wang, Y.-D. Xu, H.-Y. Chen, and J.-H. Jiang, Accidental degeneracy in photonic bands and topological phase transitions in two-dimensional core-shell dielectric photonic crystals, Opt. Express **24**, 18059 (2016).

[13] X. Zhu, H.-X. Wang, C. Xu, Y. Lai, J.-H. Jiang, and S. John, Topological transitions in continuously deformed photonic crystals, Phys. Rev. B **97**, 085148 (2018).

[14] T. Ma and G. Shvets, All-Si valley-Hall photonic topological insulator, New J. Phys. **18**, 025012 (2016).

[15] X.-D. Chen, F.-L. Zhao, M. Chen, and J.-W. Dong, Valley-contrasting physics in all-dielectric photonic crystals: Orbital angular momentum and topological propagation, Phys. Rev. B **96**, 020202(R) (2017).

[16] J. Noh, S. Huang, K. P. Chen, and M. C. Rechtsman, Observation of photonic topological valley Hall edge states, Phys. Rev. Lett. **120**, 063902 (2018).

[17] M. C. Rechtsman, J. M. Zeuner, Y. Plotnik, Y. Lumer, D. Podolsky, F. Dreisow, S. Nolte, M. Segev, and A. Szameit, Photonic Floquet topological insulators, Nature (London) **496**, 196 (2013).

[18] D. Leykam, M. C. Rechtsman, and Y. D. Chong, Anomalous topological phases and unpaired Dirac cones in photonic Floquet topological insulators, Phys. Rev. Lett. **117**, 013902 (2016).

[19] F. Gao, Z. Gao, X. Shi, Z. Yang, X. Lin, H. Xu, J. D. Joannopoulos, M. Soljačić, H. Chen, L. Lu, Y. D. Chong, and B. Zhang, Probing topological protection using a designer surface plasmon structure, Nat. Commun. **7**, 11619 (2016).

[20] M. Wang, W. Zhou, L. Bi, C. Qiu, M. Ke, and Z. Liu, Valley-locked waveguide transport in acoustic heterostructures, Nat. Commun. **11**, 3000 (2020).

[21] M. Wang, R.-Y. Zhang, L. Zhang, D. Wang, Q. Guo, Z.-Q. Zhang, and C. T. Chan, Topological one-way large-area waveguide states in magnetic photonic crystals, Phys. Rev. Lett. **126**, 067401 (2021).

[22] X. Yu, J. Chen, Z.-Y. Li, and W. Liang, Topological large-area one-way transmission in pseudospin-field-dependent waveguides using magneto-optical photonic crystals, Photon. Res. **11**, 1105 (2023).

[23] L. He, Z. Lan, B. Yang, J. Yao, Q. Ren, J. You, W. E. I. Sha, Y. Yang, and L. Wu, Experimental observation of topological large-area pseudo-spin-momentum-locking waveguide states with exceptional robustness, Adv. Photon. Nexus **3**, 016009 (2024).

[24] Q. Chen, L. Zhang, F. Chen, Q. Yan, R. Xi, H. Chen, and Y. Yang, Photonic topological valley-locked waveguides, ACS Photonics **8**, 1400 (2021).

[25] H. Shao, Y. Wang, G. Yang, and T. Sang, Topological transport in heterostructure of valley photonic crystals, Opt. Express **31**, 32393 (2023).

[26] S. Li, M. L. N. Chen, Z. Lan, and P. Li, Coexistence of large-area topological pseudospin and valley states in a tri-band heterostructure system, Opt. Lett. **48**, 4693 (2023).

[27] Q. Chen, L. Zhang, M. He, Z. Wang, X. Lin, F. Gao, Y. Yang, B. Zhang, and H. Chen, Valley-Hall photonic topological insulators with dual-band kink states, Adv. Opt. Mater. **7**, 1900036 (2019).

[28] Z. Lan, J. W. You, and N. C. Panoiu, Nonlinear one-way edge-mode interactions for frequency mixing in topological photonic crystals, Phys. Rev. B **101**, 155422 (2020).

[29] Z. Lan, J. W. You, Q. Ren, W. E. I. Sha, and N. C. Panoiu, Second-harmonic generation via double topological valley-Hall kink modes in all-dielectric photonic crystals, Phys. Rev. A **103**, L041502 (2021).

[30] G.-C. Wei, Z.-Z. Liu, D.-S. Zhang, and J.-J. Xiao, Frequency dependent wave routing based on dual-band valley-Hall topological photonic crystal, New J. Phys. **23**, 023029 (2021).

[31] H. Xing, G. Xu, D. Lu, J. Fan, Z. Xue, Z. Gao, and L. Cong, Terahertz topological photonic crystals with dual edge states for efficient routing, Opt. Lett. **48**, 2805 (2023).

[32] M. L. N. Chen, L. J. Jiang, Z. Lan, and W. E. I. Sha, Coexistence of pseudospin- and valley-Hall-like edge states in a photonic crystal with C_{3v} symmetry, Phys. Rev. Res. **2**, 043148 (2020).

[33] G. Wei, Z. Liu, L. Wang, J. Song, and J.-J. Xiao, Coexisting valley and pseudo-spin topological edge states in photonic topological insulators made of distorted Kekulé lattices, Photonics Res. **10**, 999 (2022).

[34] Y. Wang, H.-X. Wang, L. Liang, W. Zhu, L. Fan, Z.-K. Lin, F. Li, X. Zhang, P.-G. Luan, Y. Poo, J.-H. Jiang, and G.-Y. Guo, Hybrid topological photonic crystals, Nat. Commun. **14**, 4457 (2023).

[35] W. A. Benalcazar, T. Li, and T. L. Hughes, Quantization of fractional corner charge in C_n-symmetric higher-order topological crystalline insulators, Phys. Rev. B **99**, 245151 (2019).

[36] Y. Li, Y. Yu, F. Liu, B. Zhang, and G. Shvets, Topology-controlled photonic cavity based on the near-conservation of the valley degree of freedom, Phys. Rev. Lett. **125**, 213902 (2020).